Evidence for $\omega' \to \omega\sigma$ and $b_1(1235)\pi$

A.V. Anisovich [c], C.A. Baker [a], C.J. Batty [a], D.V. Bugg [b], C. Hodd [b], V.A. Nikonov [c], A.V. Sarantsev [c], V.V. Sarantsev [c], B.S. Zou [b,1]

[a] *Rutherford Appleton Laboratory, Chilton, Didcot OX11 0QX, UK*

[b] *Queen Mary and Westfield College, London E1 4NS, UK*

[c] *St. Petersburg Nuclear Physics Institute, Gatchina, St. Petersburg district, Russia 188350*

Abstract

Data are presented on $\bar{p}p \to \omega\pi^0\pi^0\pi^0$ at rest in gaseous and liquid hydrogen. These data fit naturally to ${}^1P_1(\bar{p}p) \to [\omega'(1420)\pi^0]_{L=0}$ and ${}^3S_1(\bar{p}p) \to [\omega'(1420)\pi^0]_{L=1}$, with $\omega'(1420) \to \omega\sigma$ and $b_1(1235)\pi^0$. However, the width fitted to ω', $\Gamma = 360^{+100}_{-60}$ MeV, is larger than earlier estimates.

[1] Now at the Institute for High Energy Physics, Beijing 100039, China

Antonelli et al. [1] have reported evidence for $\omega'(1420)$ in DM2 data on $e^+e^- \to \rho\pi$. The identification depends on interference between $\omega'(1420)$ and $\omega'(1600)$. Since this is the only observation of $\omega'(1420)$ to date, confirmation is desirable. A comprehensive review of ρ' and ω' states in the mass range 1200–1700 MeV has been given by Clegg and Donnachie [2]. The $\omega'(1420)$ may be interpreted as the isospin 0 partner of $\rho'(1450)$.

Here we present data taken at LEAR by the Crystal Barrel collaboration on $\bar{p}p$ at rest $\to \omega\pi^0\pi^0\pi^0$, $\omega \to \pi^0\gamma$, i.e. 9γ data. These data have been taken both in liquid hydrogen and gaseous hydrogen, making possible a determination of the relative amounts of annihilation through $\bar{p}p$ S– and P–states.

The experimental set-up has been described in a full technical report [3]. Anti-protons are brought to rest in targets of liquid or gaseous hydrogen at the centre of the Crystal Barrel detector. The gaseous target was operated at 12 atmospheres pressure and room temperature. Immediately around the target are multiwire and jet drift chambers, used here to veto charged particles over 98% of the solid angle. Photons are detected in a barrel of 1380 CsI crystals which also cover 98% of 4π. They have an angular resolution of ± 20 mrad in both azimuth and polar angle. The efficiency remains high down to a shower energy of 20 MeV; this is important, since the kinematics of $\omega \to \pi^0\gamma$ allow photons down to this energy. One layer of crystals immediately around the beam-pipe is used only as a veto, because some shower energy may escape from this layer into the beam pipe; this reduces the solid angle for good γ detection to 95% of 4π. The resolution in photon energy E is given by $\Delta E/E = 2.5\%/E(GeV)^{1/4}$.

The photon reconstruction follows standard procedures reported in many earlier Crystal Barrel publications, e.g. [3]. A shower is reconstructed from any cluster consisting of a central crystal and 8 immediate neighbours. Roughly 10% of showers give rise to a separate parasitic photon below 100 MeV, produced by Compton scattering out of the primary shower. These so-called 'split-offs' are rejected, and only events with nine clean showers are used. This procedure is necessary so as to minimise background from the prolific $5\pi^0 \to 10\gamma$ process, which produces many events with one low energy photon and nine other showers.

Events are first fitted kinematically to 9γ, requiring a confidence level (CL) cut $> 10\%$. Then photons are paired to π^0, and a kinematic fit to $4\pi^0\gamma$ is required, again with $CL > 10\%$. Events due to $\omega\eta$, $\eta \to \pi^0\pi^0\pi^0$ are rejected if they have a $CL > 10\%$. Fig. 1 illustrates the ω peak observed in $\pi^0\gamma$ combinations at this step. Background under the ω peak comes partially from wrong combinations with other π^0 in the event; much of this background is eliminated by the subsequent kinematic fit to $\omega\pi^0\pi^0\pi^0$.

Table 1 shows statistics at each successive step of the selection procedure. Eventually 2357 events are selected from liquid data and 2738 from gas. After correction for background discussed below and for the branching ratios of $\omega \to \pi^0\gamma$ and $\pi^0 \to \gamma\gamma$, branching fractions for $\bar{p}p \to \omega\pi^0\pi^0\pi^0$ are $(0.44 \pm 0.04)\%$ in liquid hydrogen and $(0.82 \pm 0.08)\%$ in hydrogen gas. Here, we have made use of the results that $(3.32 \pm 0.28)\%$ of annihilation in gas gives rise to neutral final states and $(3.14 \pm 0.25)\%$ in liquid [4].

Kinematic fit	gas data	liquid data	Monte Carlo
Triggers	2.12×10^6	3.89×10^6	84000
9γ	15091	11182	15355
$4\pi^0\gamma$	7054	5407	9349
no $\eta \to 3\pi^0$	6035	5009	8764
$\omega 3\pi^0$	2357	2738	4200

Table 1
Statistics of the data selection.

A Monte Carlo simulation using GEANT is used to study background from $5\pi^0$ (and other processes) and wrong combinations of $\pi^0\gamma$. The only significant surviving background is from $5\pi^0$ events where one photon escapes detection. This may be because (i) showers overlap, (ii) one photon is below the 20 MeV cut which is imposed to eliminate noise, or (iii) one photon is lost down the beam-pipe. In order to optimise the signal/background ratio, a CL cut of 55% in applied for the final kinematic fit to $\omega\pi^0\pi^0\pi^0$. (It has been checked that lower confidence level cuts do not alter the fitted physics, though backgrounds increase). After this cut, wrong combinations selected as $\omega \to \pi^0\gamma$ are estimated to be 6%. The surviving background levels are estimated to be 8% in gaseous hydrogen and 17% in liquid hydrogen. This difference in background arises mostly from the fact that the signal is stronger in gas than in liquid by a factor $r_{G/L} = 1.85 \pm 0.19$.

Figs. 2 and 3 (a)–(d) show mass distributions for $\pi^0\pi^0$, $3\pi^0$, $\omega\pi^0$ and $\omega\pi^0\pi^0$ for gaseous and liquid data. Dashed curves show $\omega\pi^0\pi^0\pi^0$ phase space after acceptance cuts. There is a broad peak above phase space in the mass spectrum of $\omega\pi^0\pi^0$ at ~ 1500 MeV, Figs. 2(d) and 3(d). There is also an enhancement in $M(\omega\pi^0)$ at the $b_1(1235)$, and a peaking at the top end of the 3π mass spectrum. All these features are important in the fit discussed below and shown by the full curves on Figs. 2 and 3. The $\pi^0\pi^0$ mass distribution in Fig. 2(a) is enhanced slightly towards the higher masses by the well known $\pi\pi$ S-wave interaction, denoted here by σ. For completeness, Figs. 2(f) and 3(f) show the Dalitz plot for $\omega\pi^0\pi^0$ combinations in the mass range 1350–1650 MeV; however, these Dalitz plots do not reveal any distinctive physics, such as $b_1(1235)$ bands.

Five pairs of processes fitted to the data are:

$$
\begin{aligned}
&{}^3S_1(\bar{p}p) \to [\rho'(1450)\sigma]_{L=0},\ \rho' \to [\omega\pi]_{\ell=1} && (1)\\
&{}^1P_1(\bar{p}p) \to [\rho'(1450)\sigma]_{L=1} && (2)\\
&{}^1P_1(\bar{p}p) \to [\omega'\pi^0]_{L=0},\ \omega' \to [\omega\sigma]_{\ell=0} && (3)\\
&{}^3S_1(\bar{p}p) \to [\omega'\pi^0]_{L=1} && (4)\\
&{}^1P_1(\bar{p}p) \to [\omega'\pi^0]_{L=0},\ \omega' \to [b_1(1235)\pi]_{\ell=0} && (5)\\
&{}^3S_1(\bar{p}p) \to [\omega'\pi^0]_{L=1} && (6)\\
&{}^1P_1(\bar{p}p) \to [\pi'(1300)\omega]_{L=0},\ \pi' \to [\pi\sigma]_{\ell=0} && (7)\\
&{}^3S_1(\bar{p}p) \to [\pi'(1300)\omega]_{L=1} && (8)\\
&{}^1P_1(\bar{p}p) \to [b_1(1235)\sigma]_{L=0},\ b_1 \to [\omega\pi]_{\ell=0} && (9)\\
&{}^3S_1(\bar{p}p) \to [b_1(1235)\sigma]_{L=1}. && (10)
\end{aligned}
$$

The general form of the amplitudes is illustrated by those for channels 1 and 2:

$$F = \Lambda e^{i\phi} V\ f(\rho') f(\sigma) B_L(q) B_\ell(k) e^{-\alpha q^2} e^{-\alpha k^2}. \tag{11}$$

Here $B_1(q) = q/\sqrt{q^2 + 1/R^2}$ is the Blatt-Weisskopf centrifugal barrier with radius R for the production process with orbital angular momentum $L = 1$; ℓ is the angular momentum in the decay; q is the momentum of the ρ' in the $\bar{p}p$ system, and k the momentum of the ω in the ρ' rest frame. The spin dependence of the amplitudes is contained in V; $f(\rho')$ is a Breit-Wigner amplitude with constant width for the ρ'; the parametrisation of Zou and Bugg [5] is used for the $\pi\pi$ S-wave amplitude σ. The exponentials are form factors using $\alpha = 1.5$ GeV^{-2} and approximating closely the Vandermeulen form factor [6]; they improve the fit marginally.

The ${}^3S_1$ contributions are determined essentially by liquid data and ${}^1P_1$ contributions by gaseous data. Earlier experience [7] is that the population of atomic S-states in liquid is $\sim 90\%$ and that of atomic P-states is $\sim 10\%$; in gas, the ratio of populations is $\sim 50 : 50$. The ratio $r_{G/L}$ of annihilation in gas and liquid is given by $0.5(b_S + b_P)/(0.9b_S + 0.1b_P)$, where $b_{S,P}$ are the branching fractions for annihilation in gas from ${}^3S_1$ and ${}^1P_1$. We require that the population of P-states is a factor 9 lower in liquid than in gas. The only effect of this constraint is to fix small amounts of P-state annihilation in liquid from the values fitted in gas.

For channels 1 and 2, ${}^3S_1$ annihilation is stronger than for ${}^1P_1$ because of the $L = 1$ centrifugal barrier in channel 2; the converse applies to pairs of channels 3–10. The fact that $r_{G/L} = 1.85 \pm 0.19$ is significantly above 1 requires that channels 1 and 2 make weak contributions compared with channels 3–10.

Phases ϕ are are fitted freely. We search initially for a solution using the constraint that

$$\Lambda(^3S_1) \simeq \Lambda(^1P_1); \tag{12}$$

that is, matrix elements for S and P state annihilation have similar magnitudes apart from the centrifugal barrier factors. We find that the fit follows this constraint naturally. The radius R of the centrifugal barrier is senstitive to relative amounts of S and P-state annihilation and optimises at 0.6 fm. The constraint (12) eliminates solutions with wildly different values of coupling constants Λ for $^3S_1$ and $^1P_1$; if this constraint is satisfied within a factor 3 for all channels, only a single solution survives. Without this constraint, it is possible for one channel to drop out of the solution completely in $^1P_1$ annihilation, but the overall character of the solution changes little.

Contributions to the fit from individual processes are shown in Figs. 4 and 5. The broad peak in the $\omega\pi\pi$ mass spectrum is not a distinctive feature of channels 3–6, but is similar in Figs 4 and 5 for all pairs of channels. Antonelli et al. quote a mass for ω' of 1419 ± 31 MeV and a width of 174 ± 59 MeV. Fig. 6 shows the $\omega\pi\pi$ mass spectrum with these values. This peak is obviously too narrow to agree with present data. A free fit to its width gives a value of $\Gamma = 360^{+100}_{-60}$ MeV and a mass of 1370 MeV with a statistical error of ± 25 MeV. The peak in the $\omega\pi\pi$ mass spectrum lies significantly above this because of the rapid increase in the phase space for $\omega\sigma$ and the proximity of the threshold for $b_1(1235)\pi$.

With this mass and width, contributions from ω' decaying to $\omega\sigma$ and $b_1(1235)\pi$ fit most features observed in Figs. 4 and 5; this is shown by the full curves. However, the peak in 3π is not well reproduced in gas, Fig. 4(b). This requires a contribution from reactions (7) and (8), $\pi'(1300)\omega$. We adopt the PDG mass of 1300 MeV for $\pi'(1300)$, though the fit is not sensitive to this value. Its width optimises at 200 ± 60 MeV; however, this width refers to a mass of ~ 1 GeV, and the width on resonance may be higher because of the increasing phase space for 3π decays.

The $b_1(1235)$ in $\omega\pi$, Figs. 4(c) and 5(c) requires contributions from both $b_1(1235)\sigma$ and $\omega' \to b_1\pi$. Panels (e) of Figs. 2 and 3 show the distribution in angle α for the decay of ω' to $\omega\sigma$ in the ω' rest frame, with respect to the direction of production of the ω'; small fluctuations are due to acceptance variations. Events are selected in the $\omega\pi\pi$ mass range 1350–1650 MeV. The dependence on $\cos\alpha$ is important in fixing contributions from channels 3–10. Both processes involving the $b_1(1235)$ produce an angular distribution falling towards $\cos\alpha = 1$, as illustrated by the dotted curves in Figs. 4(e) and 5(e), Those for $\pi'(1300)\omega$ rise towards $\cos\alpha = 1$ (dashed curves). The precise shapes of these angular distributions are not obvious, but emerge after the cut on $\omega\pi\pi$ mass and after allowing for (a) interferences between three combinations of π^0, (b) the D/S ratio for $b_1(1235)$, which is fixed to the value 0.29

quoted by the Particle Data Group [8]. In order to fit the $\cos\alpha$ distributions, some compensation is required between the b_1 contributions and $\pi'(1300)\omega$; the latter also helps fit the 3π mass distribution. The angular dependence of the decay $\omega \to \pi^0\gamma$ gives information on the helicity of the ω. However, such angular information cannot be displayed readily.

Table 2 shows changes in log likelihood when pairs of channels are dropped from the fit and remaining contributions are re-optimised. Our definition of log likelihood is such that it changes by 0.5 when one parameter changes by one standard deviation. The changes shown in Table 2 are therefore highly significant, except for channels 1 and 2, which play only a small role.

Channel	ΔS
1+2	2
3+4	341
5+6	661
3+4+5+6	882
7+8	388
9+10	467

Table 2
Changes in log likelihood S when pairs of channels are dropped from the fit and others are re-optimised.

Table 3 shows branching fractions of each channel in liquid and gas for the best fit. Systematic errors are estimated from a variety of fits with differing ingredients. The resulting error on the branching fractions of channels 1 and 2 are $\sim 50\%$ of their magnitudes. Errors on other branching fractions are $\sim 20\%$ of their magnitudes. We find that the relative decay branching ratios to $\omega\sigma$ and $b_1(1235)\pi$ are stable at the value

$$\frac{BR[\omega' \to \omega\sigma]}{BR[\omega' \to b_1(1235)\pi]} = 0.60 \pm 0.16. \tag{13}$$

The one feature of the data which is not reproduced well is the $\pi\pi$ mass spectrum in Fig. 3(a). In gas, Fig. 2(a), it peaks significantly towards the higher masses because of the $\pi\pi$ S-wave interaction σ. In liquid, Fig. 3(a), it is surprising that it follows phase space closely. No variant in the fit is capable of reproducing this feature precisely. As Figs. 4(a) and 5(a) show, the contribution from ω' alone reproduces the 2π mass distribution well, but does not quite fit the 3π mass spectrum in Fig. 5(b). The effect of the $\pi'(1300)$ contribution is to cause the small systematic discrepancy shown in Fig. 3(a).

We have tried a further possible contribution to the fit from $b_1'\sigma$, where b_1' is the radial excitation of $b_1(1235)$, decaying with $\ell = 0$ to $\omega\pi$. It is expected to

Initial State	Channel	gas	liquid
$^3S_1$	1	2	7
	4	4	13
	6	7	21
	8	2	6
	10	5	14
$^1P_1$	2	1	0.5
	3	17	5
	5	24	7.5
	7	11	3
	9	19	6
Background		8	17

Table 3
Percentage contributions to each channel.

have a mass ≥ 1540 MeV, and there is indeed evidence for it at this mass [9] from the E852 experiment. In present data, we find no significant contribution. It is likely to be suppressed by the high mass of the b_1' and the requirement that it is produced with the σ.

We have also searched for exotic 2^{+-} and 0^{+-} mesons decaying through $\omega\sigma$ with $\ell = 1$. Such states would be produced from the initial state $^1P_1$ with $L = 1$. Strong production through $^1P_1$ annihilation with $L = 1$ is implausible and we find no significant contribution.

In summary, the data require a significant contribution from ω' decaying via $\omega\sigma$ and $b_1(1235)\pi$, but with a width much larger than that of Antonelli et al. Without these contributions, log likelihood is worse by large amounts. The fit also requires some contribution from $\bar{p}p \to b_1\sigma$ and $\pi'(1300)\omega$, though the $\pi'(1300)$ is produced below resonance and its parameters cannot be determined with any precision. The $\omega\pi\pi$ mass spectrum observed here is quite different to that observed by Antonelli et al. [1] in $e^+e^- \to \omega\pi^+\pi^-$. Their spectrum peaks at 1660 MeV and rises continuously over the mass range 1400–1600 MeV. Such a spectrum fails completely to fit the present data. The difference may arise from suppression of $\omega(1600)$ in $\bar{p}p$ annihilation by the phase space restriction on $\bar{p}p \to \omega'\pi$, or it could be due to interference with $\omega'(1600)$, as Antonelli et al. propose in e^+e^-.

Finally, we comment on the systematic uncertainty in the mass of $\omega'(1420)$. The mass 1370 ± 25 MeV quoted above is for a simple Breit-Wigner amplitude of constant width. The decay modes observed so far are to $\rho\pi$, $\omega\sigma$ and $b_1(1235)\pi$. The phase space for these processes peaks towards the higher masses. In principle, this mass dependence should be included in the width $\Gamma(s)$ of the resonance. The increase of $\Gamma(s)$ in the Breit-Wigner denominator will reduce the amplitude at high mass, and will lead to some increase in the mass fitted to the resonance. Unfortunately, lack of information on the relative branching ratio to $\rho\pi$ prevents an accurate assessment of this effect at present. Trials have been made with a variety of branching ratios. We find that the mass may increase to 1420 or, less likely, to 1450 MeV. Our experience elsewhere [10] is that the mass of 1370 MeV fitted with a simple Breit-Wigner amplitude of constant width approximates the pole position, whatever the $s-$dependence of $\Gamma(s)$.

1 Acknowledgement

We thank the Crystal Barrel collaboration for the use of these data. We wish to thank the technical staff of the LEAR machine group and of all the participating institutions for their invaluable contributions to the success of the experiment. We acknowledge financial support from the British Particle Physics and Astronomy Research Council (PPARC). The St. Petersburg group wishes to acknowledge financial support from PPARC and INTAS grant RFBR 95-0267.

References

[1] A. Antonelli et al., Zeit. Phys. C56 (1992) 15.

[2] A.B. Clegg and A. Donnachie, Zeit. Phys. C62 (1994) 455.

[3] E. Aker et al., Nucl. Instr. A321 (1992) 69.

[4] M. Herz, University of Bonn, Dissertation (1997).

[5] B.S. Zou and D.V. Bugg, Phys. Rev. D48 (1993) R3948.

[6] J. Vandermeulen, Z. Phys. C37 (1988) 563.

[7] C.J. Batty, Nucl. Phys. A601 (1996) 425.

[8] Particle Data Group, Euro. Phys. J. C3 (1998) 1. 322.

[9] P. Eugenio. Ph.D. thesis, University of Mass., Amherst(1998).

[10] D.V. Bugg, A.V. Sarantsev and B.S. Zou, Nucl. Phys. B471 (1996) 59.

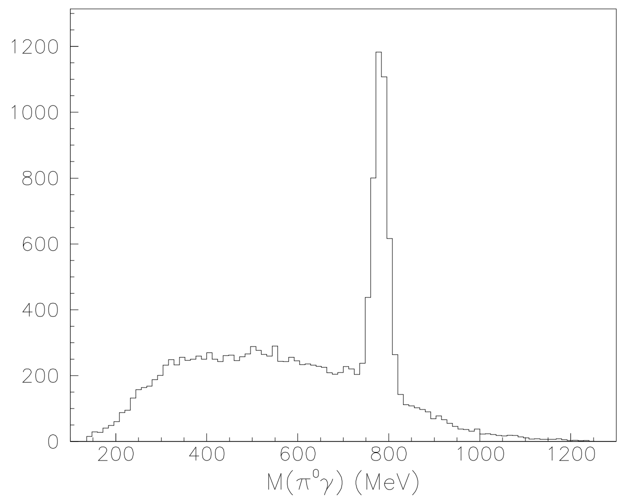

Fig. 1. The spectrum of $\pi^0\gamma$ masses in data from hydrogen gas after a kinematic fit to $4\pi^0\gamma$.

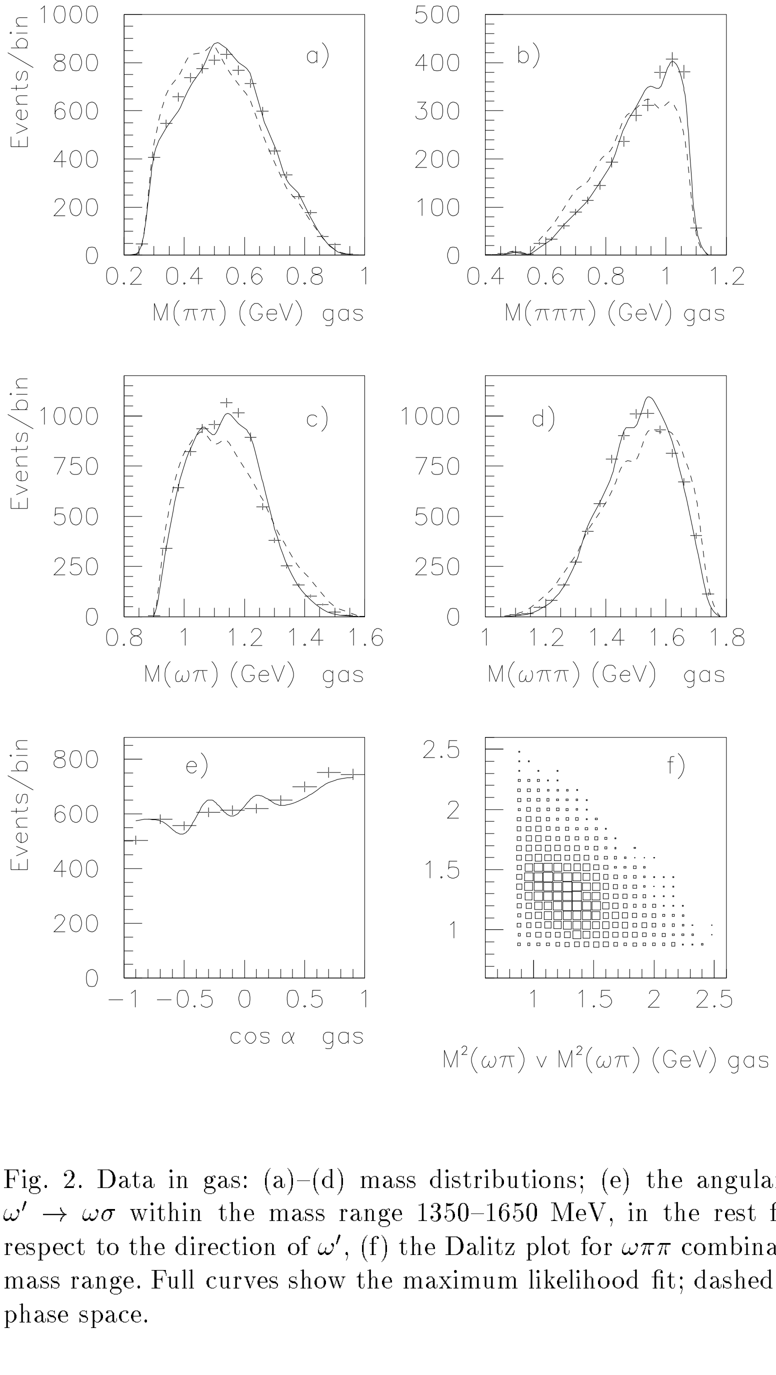

Fig. 2. Data in gas: (a)–(d) mass distributions; (e) the angular distribution for $\omega' \to \omega\sigma$ within the mass range 1350–1650 MeV, in the rest frame of ω', with respect to the direction of ω', (f) the Dalitz plot for $\omega\pi\pi$ combinations in the same mass range. Full curves show the maximum likelihood fit; dashed curves show $\omega 3\pi$ phase space.

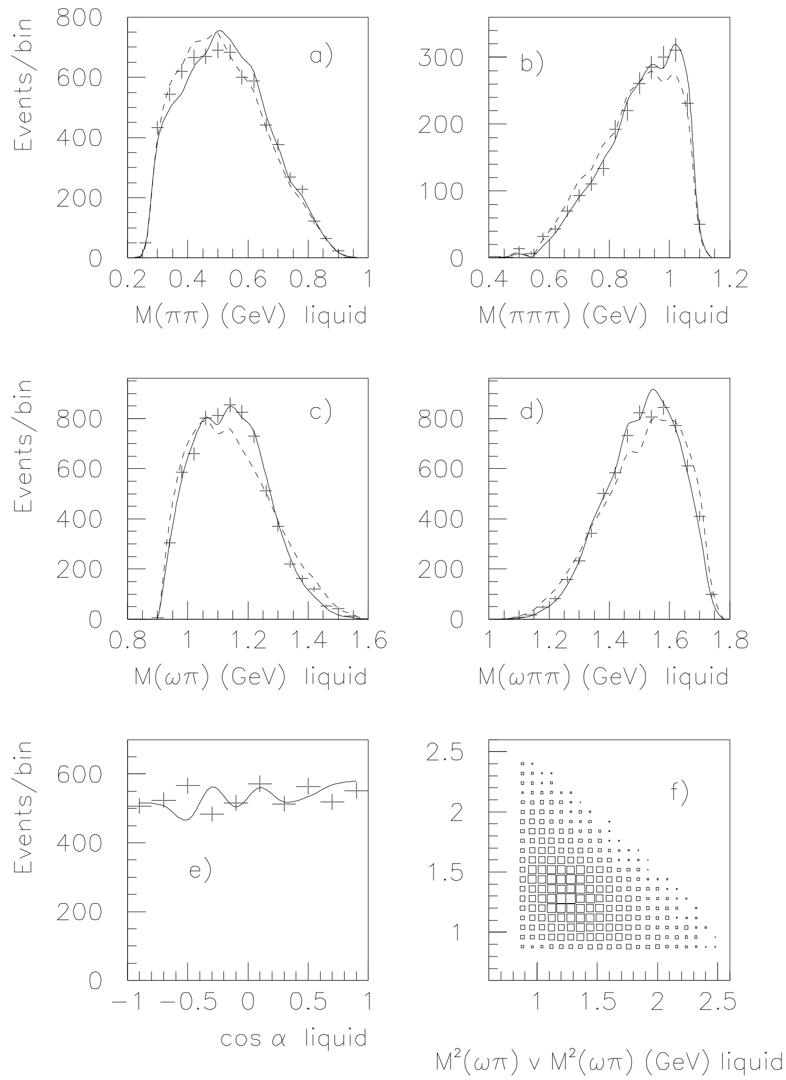

Fig. 3. As Fig. 2 for data in liquid hydrogen.

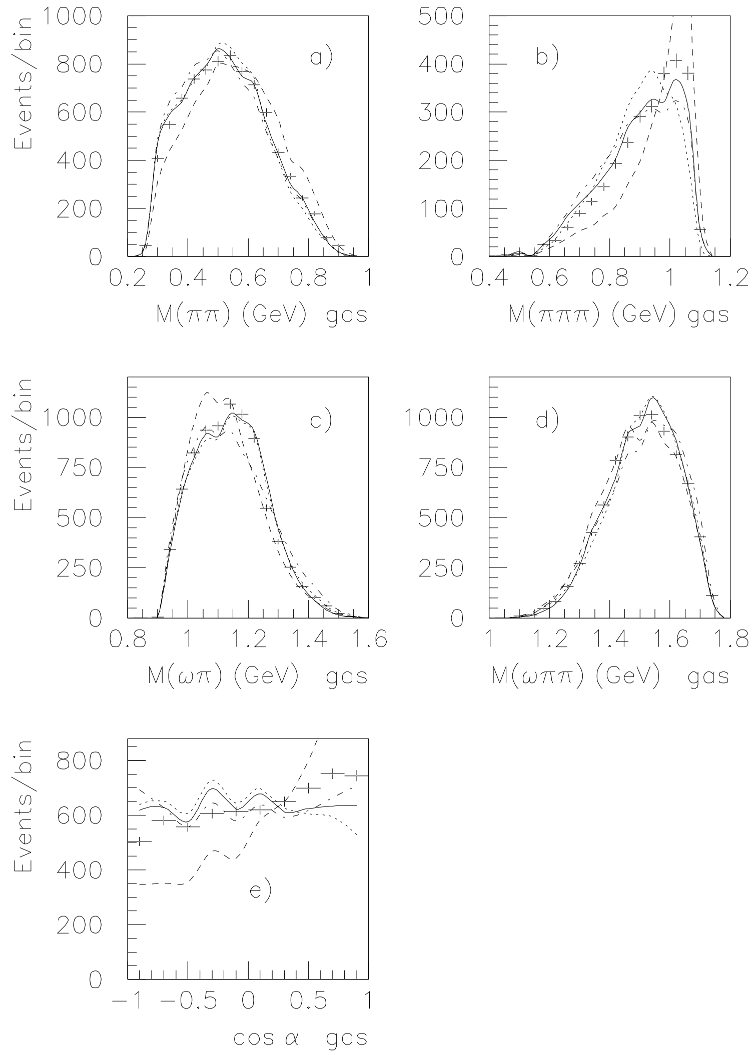

Fig. 4. Comparison with gas data of predictions for $\bar{p}p \to \omega'\pi$ (full curves), $b_1(1235)\sigma$ (dotted), $\pi'(1300)\omega$ (dashed), and $\rho'\sigma$ (chain curve). All are normalised to the total number of events in the data.

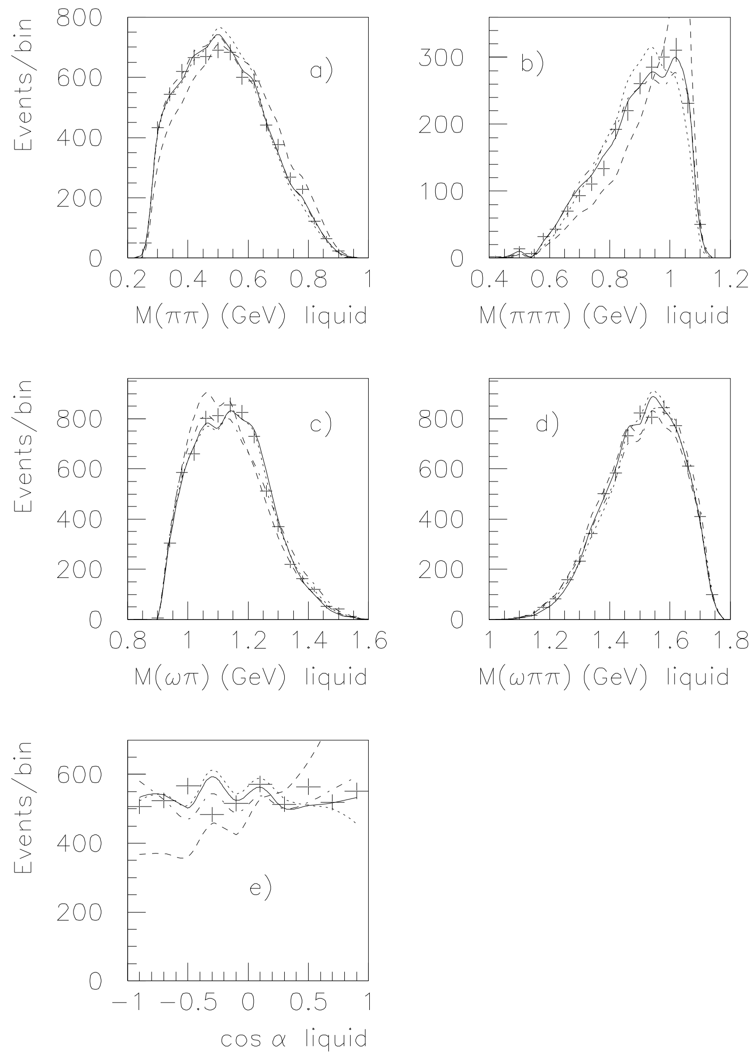

Fig. 5. As Fig. 4 for data from liquid hydrogen.

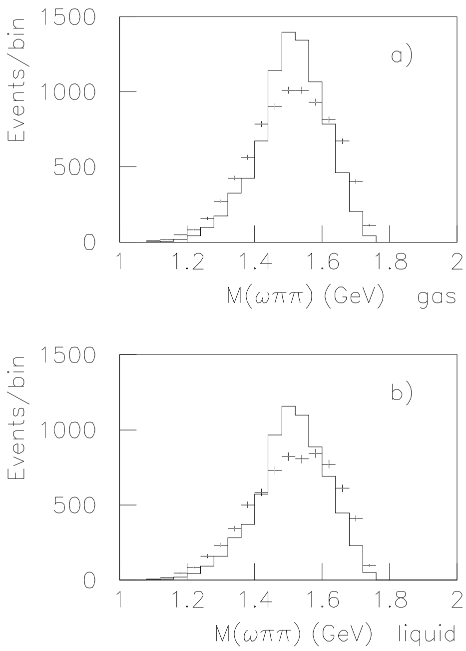

Fig. 6. Predicted spectra (full histograms) for $\omega' \rightarrow \omega\pi\pi$ with the ω' mass and width of Antorelli et al. compared with data (crosses).